Materials Today Bio 13 (2022) 100198

Contents lists available at ScienceDirect

Materials Today Bio

journal homepage: www.journals.elsevier.com/materials-today-bio

# Self-assembled porphyrin polymer nanoparticles with NIR-II emission and highly efficient photothermal performance in cancer therapy

Cheng Li [a,1], Zijin Luo [a,1], Lixia Yang [a,1], Jun Chen [b,**], Kai Cheng [c], Yanan Xue [a], Genyan Liu [a], Xiaogang Luo [a,d], Fengshou Wu [a,*]

[a] Hubei Key Laboratory of Novel Reactor and Green Chemical Technology, Key Laboratory for Green Chemical Process of Ministry of Education, School of Chemical Engineering and Pharmacy, Wuhan Institute of Technology, Wuhan, 430072, PR China
[b] School of Chemistry and Environmental Engineering, Wuhan Institute of Technology, Wuhan, 430072, PR China
[c] College of Life Science and Technology, Huazhong University of Science and Technology, Wuhan, 430074, Hubei, PR China
[d] School of Materials Science and Engineering, Zhengzhou University, Zhengzhou, 450001, PR China

ARTICLE INFO

*Keywords:*
Porphyrin
Photothermal therapy
Self-assembly
Polymer
NIR-II

ABSTRACT

The development of new organic nanoagents with extremely high photothermal conversion efficiency and good biocompatibility has gained considerable attention in the area of photothermal cancer therapy. In this work, we designed and synthesized a new porphyrin polymer (P-PPor) with donor-acceptor (D-A) structure. P-PPor displayed intense absorbance in the near-infrared (NIR) region with the maximum peak around at 850 nm. Under excitation of 808 nm, P-PPor demonstrated the significant fluorescence in the NIR-II region ($\lambda_{max}$ = 1015 nm), with the fluorescence quantum yield of 2.19%. Due to the presence of hydrophilic PEG chains and hydrophobic alkyl chains in the conjugated skeleton, the amphiphilic P-PPor could self-assemble into the nanoparticles (P-PPor NPs) with good dispersibility in water and enhanced absorption in the NIR region. Moreover, P-PPor NPs exhibited quenched fluorescence because of the aggregation-caused quenching (ACQ) effect, resulting in the distinct photothermal effect. The photothermal conversion efficiency (PCE) of P-PPor NPs was measured as 66% under 808 nm laser irradiation, higher than most of PTT agents. The remarkable photothermal effect of P-PPor NPs was further demonstrated in vitro and in vivo using 4T1 tumor mode. Meanwhile, the NIR-II fluorescence imaging in vivo indicated the high distribution of P-PPor NPs in tumor site. These results suggested that P-PPor NPs could effectively damage the cancer cells in mice under 808 nm laser irradiation, and did not cause any obvious side effects after phototherapy. Thus, P-PPor NPs could be used as a potential agent in photothermal cancer therapy with high effectiveness and safety.

## 1. Introduction

Cancer has become one of the biggest threats to human beings' life nowadays. Although the traditional treatment methods such as surgery, radiotherapy and chemotherapy can kill cancer cells to some extent, their severe side effects, drug resistance, and easy recurrence have severely limited their applications [1–3]. As a safe, efficient and noninvasive treatment method, phototherapy has gradually become a hot research topic [4–8]. For example, photothermal therapy (PTT) only produces a thermal effect in local to kill tumor cells under NIR light irradiation in the role of photothermal agents. Therefore, PTT is a promising tumor treatment method with the advantages of low invasiveness, simple operation, short treatment time, and quick recovery [9–12]. The effectiveness of PTT extremely relies on photothermal agents, which are essential for effectively converting light energy into heat to ablate cancer cells. So far, various photosensitive nanomaterials, such as metal-based nanomaterials [9,13], carbon-based nanomaterials [14–16] and semiconducting polymers [17–19], were demonstrated as efficient photothermal agents in PTT owing to their high photothermal conversion efficiency, intense absorption and good stability [20–23]. However, the poor pharmacokinetics, non-biodegradable characteristics, and long-term biological safety issues greatly limit their further clinical

* Corresponding author.
** Corresponding author.
*E-mail addresses:* ychenjun2006@163.com (J. Chen), wfs42@126.com (F. Wu).
[1] These authors contributed equally to this work.

https://doi.org/10.1016/j.mtbio.2021.100198
Received 19 October 2021; Received in revised form 28 December 2021; Accepted 28 December 2021
Available online 30 December 2021

applications [24,25]. Therefore, it's greatly urgent to develop organic molecule-based photothermal agents with intense NIR absorption, significant light-to-heat conversion efficiency (PCE), and good biological safety.

Porphyrin derivatives exhibit good photosensitivity, excellent biocompatibility and high stability, and tend to accumulate in tumor sites compared with normal tissues [26–29]. Therefore, they are suitable candidates in optical treatments including PTT and PDT (photodynamic therapy). However, the extreme hydrophobicity, inadequate selectivity to tumor tissues, and weak absorption in the NIR region of porphyrin derivatives limited their further applications in clinic [30,31]. Besides, the porphyrin derivatives with absorption or emission in the second near-infrared window (NIR-II, 1000–1700 nm) are rarely reported [11, 32–35]. Perylene diimide (PDI) with a large π-π conjugated system has been widely used in the area of tumor treatment due to its excellent photophysical properties and high thermal stability [36–39]. Moreover, PDI has a strong ability to withdraw electrons due to the existence of carbonyl groups. Therefore, it could conjugate with the electron donors to form the D-A structure to enhance the near-infrared absorption and photothermal effect [4,40].

Herein, we designed and synthesized a conjugated porphyrin polymer (P-PPor) with D-A structure by conjugation with porphyrin (electron donor) and perylene diimide (electron acceptor). The amphiphilic P-PPor was then transformed into the nanoparticles by self-assembly method, which further enhanced their absorption in the NIR region and dispersibility in water [41]. The self-aggregation of molecules induced the quenching of NIR fluorescence, probably ascribed to the molecule aggregation in nanostructures, thereby enhancing the photothermal effect. The PCE of P-PPor NPs was calculated as 66%, high enough for photothermal cancer therapy. Finally, the remarkable photothermal effect of P-PPor NPs was verified in vitro and in vivo using 4T1 tumor mode. Furthermore, the NIR-II fluorescence imaging in vivo indicated the high distribution of P-PPor NPs in tumor site. Thus, this work provided a new strategy for the rational design and development of safe and effective nanoagents in photothermal cancer therapy.

## 2. Results and discussion

The conjugated porphyrin polymer (P-PPor) was synthesized with porphyrin as electron donor (D) and perylene diimide as electron acceptor (A). The synthetic routes of Por and P-PPor were shown in Supporting Information. Specifically, the porphyrin 4 with two PEG chains was prepared by [2 + 2] method. After bromination at two meso-positions, complexation with zinc, and conjugation with triple bond, Por was obtained in high yield. Por was then conjugated with brominated perylene diimide (PDI) through Songashira coupling reaction to synthesize the desired polymer (P-PPor) (Fig. 1). The structure of the intermediates and Por was characterized by nuclear magnetic resonance (NMR) and mass spectrometry (MS). The structure of P-PPor was confirmed by NMR spectrum and gel permeation chromatography (GPC). The number-average molecular weight (Mn) and polydispersity index (PDI) of P-PPor were determined as 7737 and 1.716 respectively through GPC. According to the calculated molecular orbitals of P-PPor (insert Fig. 1), the HOMO and LUMO are delocalized in the backbone of porphyrin and PDI, respectively, indicating the D-A structure. Therefore, the delocalization of π electron in P-PPor induced the extremely low bandgap (1.67 eV), ensuring the strong absorbance in the near-infrared region. Subsequently, the amphiphilic P-PPor assembled into nanoparticles spontaneously without adding any extra polymeric matrix using reprecipitation method.

The dynamic light scattering (DLS) indicated the uniform distribution of P-PPor NPs in the aqueous solution, with an average size of 133 nm (Fig. 2a), facilitating the passively targeting in tumor sites through the EPR effect. The transmission electron microscopy (TEM) revealed the nanoparticles were spherical (insert Fig. 2a). The zeta potential of P-PPor NPs (Fig. 2b) was negative (−35.2 mV), indicating their good stability in the aqueous solution due to the electrostatic repulsion between nanoparticles. Besides, the average size of P-PPor NPs did not display any significant change during the storage in different solutions for several days (Fig. S1), confirming the colloidal stability of the nano solution.

The absorption and fluorescence spectra of P-PPor and P-PPor NPs were recorded in THF and water, respectively. Comparing with that of

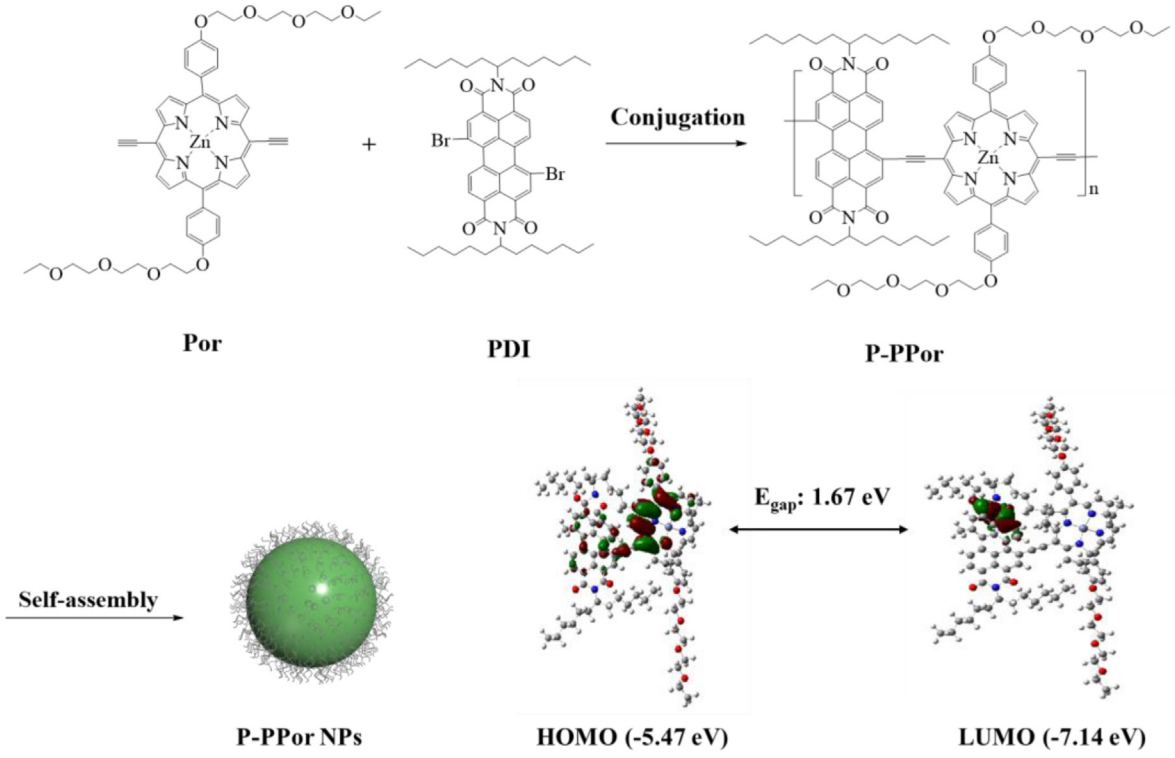


**Fig. 1.** Preparation of P-PPor and P-PPor NPs (Insert: the calculated molecular orbitals of P-PPor).

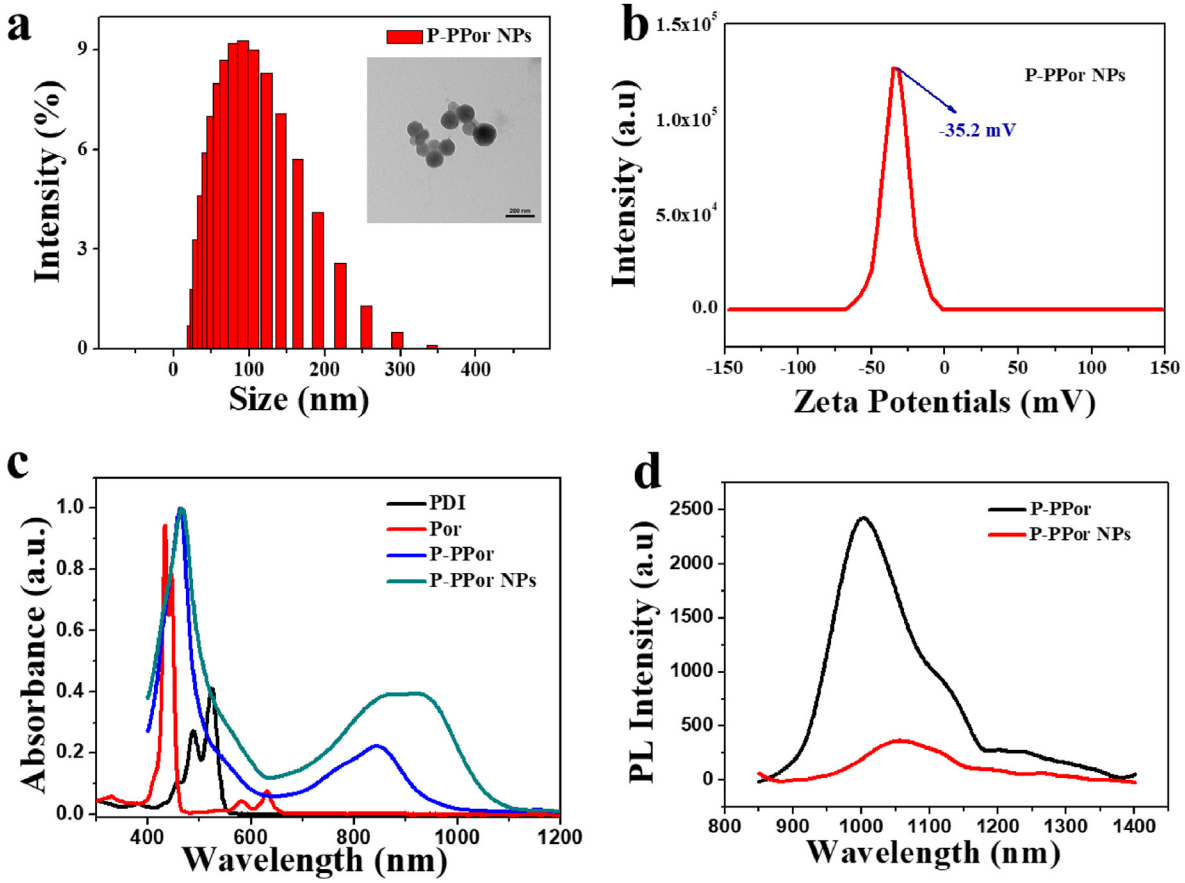


**Fig. 2.** (a) DLS profile of P-PPor NPs (Insert: TEM image of P-PPor NPs); (b) Zeta potential of P-PPor NPs; (c) UV–Vis–NIR spectra of Por, PDI, P-PPor and P-PPor NPs; (d) Near-infrared fluorescence spectra of P-PPor and P-PPor NPs ranging from 850 to 1400 nm.

Por and PDI, P-PPor displayed the broadened and red-shifted absorption spectrum, with the maximum peak at 850 nm in the near-infrared region (Fig. 2c). The extinction coefficient of P-PPor was calculated to be 7.62 L/μmol·cm (Fig. S2), indicating its good light absorption ability. After self-assembly into the related nanoparticles, the absorption of P-PPor NPs was further red-shifted and broadened, probably ascribed to the intermolecular π-π aggregation of molecules in the nanostructure. Remarkably, P-PPor displayed the significant NIR-II emission extending from 850 to 1400 nm with the maximum peak at 1015 nm (Fig. 2d). After transformation into nanoparticles, the fluorescence spectra in the NIR-II region was red-shifted and broadened, along with the fluorescence quenching to some extent. The fluorescence quantum yield of P-PPor in THF and P-PPor NPs in water was determined as 2.19% and 0.08% respectively by using IR-1061 as a reference (Fig. S3). The fluorescence quenching of nanoparticles was probably ascribed to the ACQ effect, which enhanced the non-radiative heat generation for photothermal therapy.

Because of the strong absorption in the NIR region, we measured the photothermal effect of P-PPor NPs under 808 nm laser irradiation with the change of laser power density and NPs concentration. As shown in Fig. 3a, the temperature of P-PPor NPs was significantly elevated with the increase of concentration under laser irradiation for 10 min. As a control, the pure water has little temperature increase under the same conditions. Meanwhile, the aqueous solution of P-PPor NPs exhibited laser power density-dependent temperature rise behavior. As indicated in Fig. 3b, when the concentration of P-PPor was 50 μg/mL, the solution temperature was increased by 5 °C at 0.3 W/cm$^2$, while 28 °C at 1.5 W/cm$^2$. Moreover, there was no significant change in temperature increase of P-PPor NPs after five heating/cooling cycles under 808 nm laser (Fig. 3c), confirming its high photothermal stability. The time constant (τ) for heat transfer of the system was measured as 413.9, based on the linear curve of cooling time (t) versus the negative natural logarithm of temperature (-ln θ) (Fig. 3d). According to these data, the PCE of P-PPor NPs was calculated as 66%, high enough as agent for photothermal therapy [42–44]. The photostability of P-PPor NPs was further confirmed by recording its absorption spectrum before and after laser irradiation. Comparing with that of indocyanine green (ICG) (Fig. 3e), the absorbance of P-PPor NPs did not display any significant change after laser irradiation (Fig. 3f), indicating its excellent photostability.

The biocompatibility of P-PPor NPs against normal cells (NIH-3T3) and tumor cells (4T1) were evaluated in vitro. As shown in Fig. 4a and b, the NIH-3T3 and 4T1 cells maintained over 95% survival rate when the concentration of nanoparticles reached 35 μg/mL, suggesting the low dark cytotoxicity and high biocompatibility of P-PPor NPs. After laser irradiation for 10 min (808 nm, 0.8 W/cm$^2$), the viability of cancer cells (4T1) decreased gradually with the increase of P-PPor NPs concentration (Fig. 3b). When the concentration of P-PPor NPs was elevated to 35 μg/mL, only 24.1% of cancer cells were survived, suggesting the high phototherapeutic effect of P-PPor NPs. The biocompatibility and phototherapeutic effect of P-PPor NPs were further verified through live/dead staining, where the live and dead cells were distinguished by calcein AM (green emission) and propidium iodide (PI) (red emission), respectively. As shown in Fig. 4c, almost all the 4T1 cells that treated with P-PPor NPs and laser irradiation were killed and displayed obvious red emission. In contrast, the other control groups showed bright green emission, confirming the negligible damage of bare NIR irradiation or P-PPor NPs to

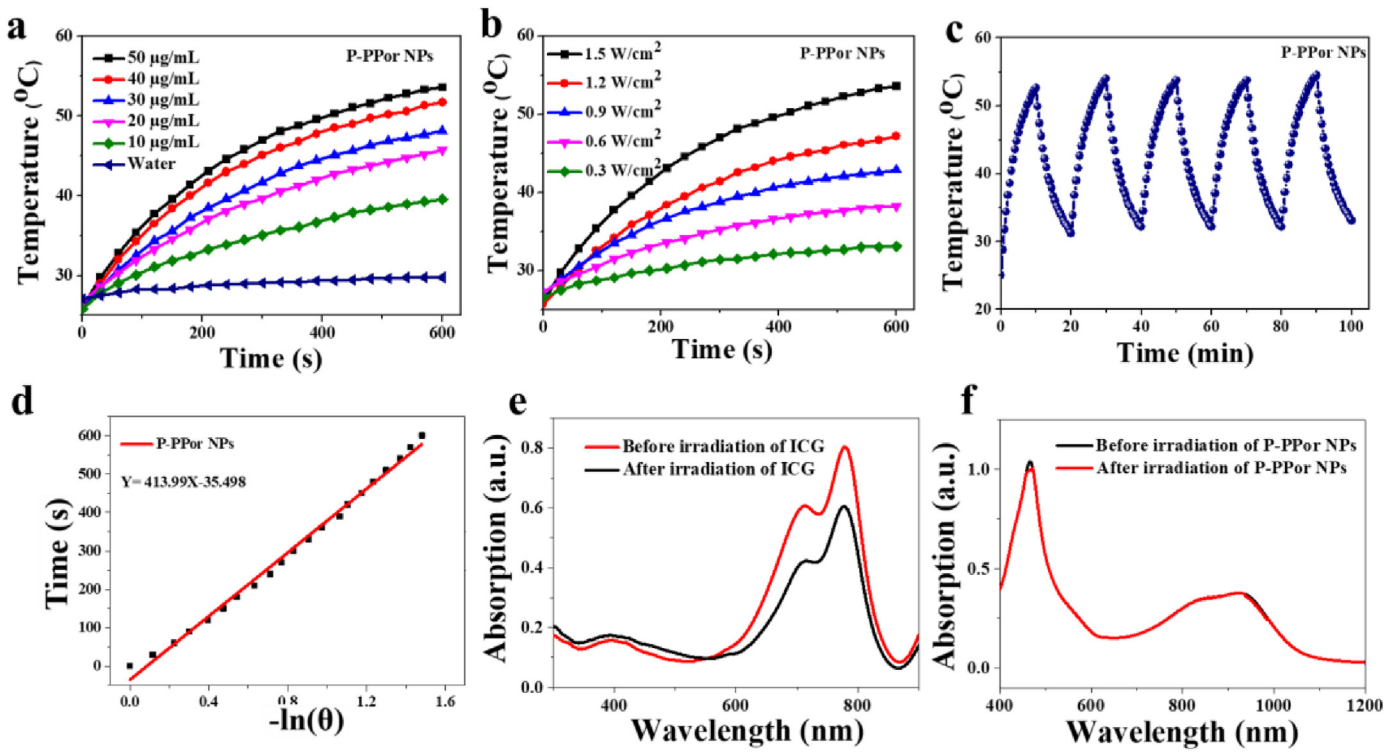


**Fig. 3.** (a) Photothermal properties of P-PPor NPs at various concentrations upon 808 nm laser (1.5 W/cm$^2$) irradiation; (b) Photothermal properties of P-PPor NPs upon laser with different power densities; (c) Photothermal properties of P-PPor NPs after five on/off irradiation cycles; (d) Linear cooling time data versus ln(θ) of P-PPor NPs in the cooling period; Absorption spectra before and after radiation of ICG (e) and P-PPor NPs (f).

cancer cells. The similar results were observed in an Annexin V-FITC/PI apoptosis assay. As shown in Fig. 4d, only 0.78% cells were still alive after treated with P-PPor NPs and laser irradiation (808 nm, 0.8 W/cm$^2$) for 10 min. While the cells in other control groups kept more than 87.36% of survival rate. These results proved that P-PPor NPs can significantly inhibit the proliferation of tumor cells, which can be used as a potential nanomaterial in PTT.

Inspired by the remarkable photothermal effect and good biocompatibility of P-PPor NPs, we then investigated the in vivo phototherapeutic efficiency using 4T1 tumor mode. As shown in Fig. 5a and b, the tumor site temperature of "P-PPor NPs + Laser" group increased from 33.4 to 55.2 °C upon laser exposure for 10 min (808 nm, 1.5 W/cm$^2$), high enough to kill cancer cells. In contrast, the temperature of control group only raised by 4.7 °C under the same irradiation, indicating that P-PPor NPs exhibited the high photothermal effect in vivo. To investigate the metabolism of P-PPor NPs in vivo, the infrared thermal images of tumor-bearing mice were taken after intravenous injection of P-PPor NPs. As indicated in Fig. 6a, the temperature of tumor site raised gradually after injection of NPs and reached the maximum at 8 h. After that, the infrared thermal signals decreased gradually due to the metabolism. Therefore, 8 h post injection was chosen as an appropriate time for laser irradiation.

Subsequently, we investigated the PTT efficiency of P-PPor NPs in vivo under 808 nm laser irradiation using 4T1 tumor-bearing mice. The mice were divided into four groups randomly, named "Saline", "Saline + Laser", "P-PPor NPs", and "P-PPor NPs + Laser", respectively. The tumor volume and weight of the mice were recorded every other day during the observation period. As shown in Fig. 6b, the tumors treated with P-PPor NPs and laser irradiation were greatly inhibited and completely eliminated after 2 days of treatment, while the tumors in other three groups constantly grew up. The photographs of mice in four groups were recorded during the observation period of 14 days. As shown in Fig. 6c, no recurrence was observed in the tumor-bearing mice treated with P-PPor NPs and 808 nm laser irradiation during the entire treatment period, indicating the high phototherapeutic efficiency of P-PPor NPs. Moreover, no obvious body weight loss was observed in mice of "Saline + Laser", "P-PPor NPs", and "P-PPor NPs + Laser" groups when compared with the control "Saline" group (Fig. 6d), suggesting the low side effect of P-PPor NPs and laser in PTT.

To investigate the in vivo bio-distribution of P-PPor NPs, 100 μL P-PPor NPs with concentration of 1 mg/mL was injected into the 4T1 tumor-bearing mice via tail vein. As illustrated in Fig. 7a, the NIR-II fluorescence signal of P-PPor NPs at the tumor region of mice was continuously increasing with the prolongation of time and reached a maximum value after iv injection for 12 h. In addition, the fluorescence signal at tumor site after iv injection was brighter than other organs, attributing to the good enrichment ability of P-PPor NPs in tumor site. The excised major organs and tumor after 48 h post-injection were then collected for the biodistribution assay. As shown in Fig. 7b, significant signal was observed in the tumor site relative to that in the lung, kidney, and heart, indicating a higher distribution of the P-PPor NPs.

To further investigate the biocompatibility of P-PPor NPs and laser irradiation, the main organs (heart, lung, spleen, kidney, liver) of each group were excised and sectioned for hematoxylin and eosin (H&E) staining after the observation period. As indicated in Fig. 8, the organ damage or inflammatory lesions were not observed in each group, indicating the negligible side effect of P-PPor NPs on the major organs. These results suggested that P-PPor NPs could be acted as an efficient and biocompatible nanoagent in photothermal cancer therapy.

In order to explore the potential long-term toxicity of P-PPor NPs in vivo, the tumor-bearing mice in four groups were sacrificed for serum biochemistry assay at 7 and 14 days after intravenous injection. As

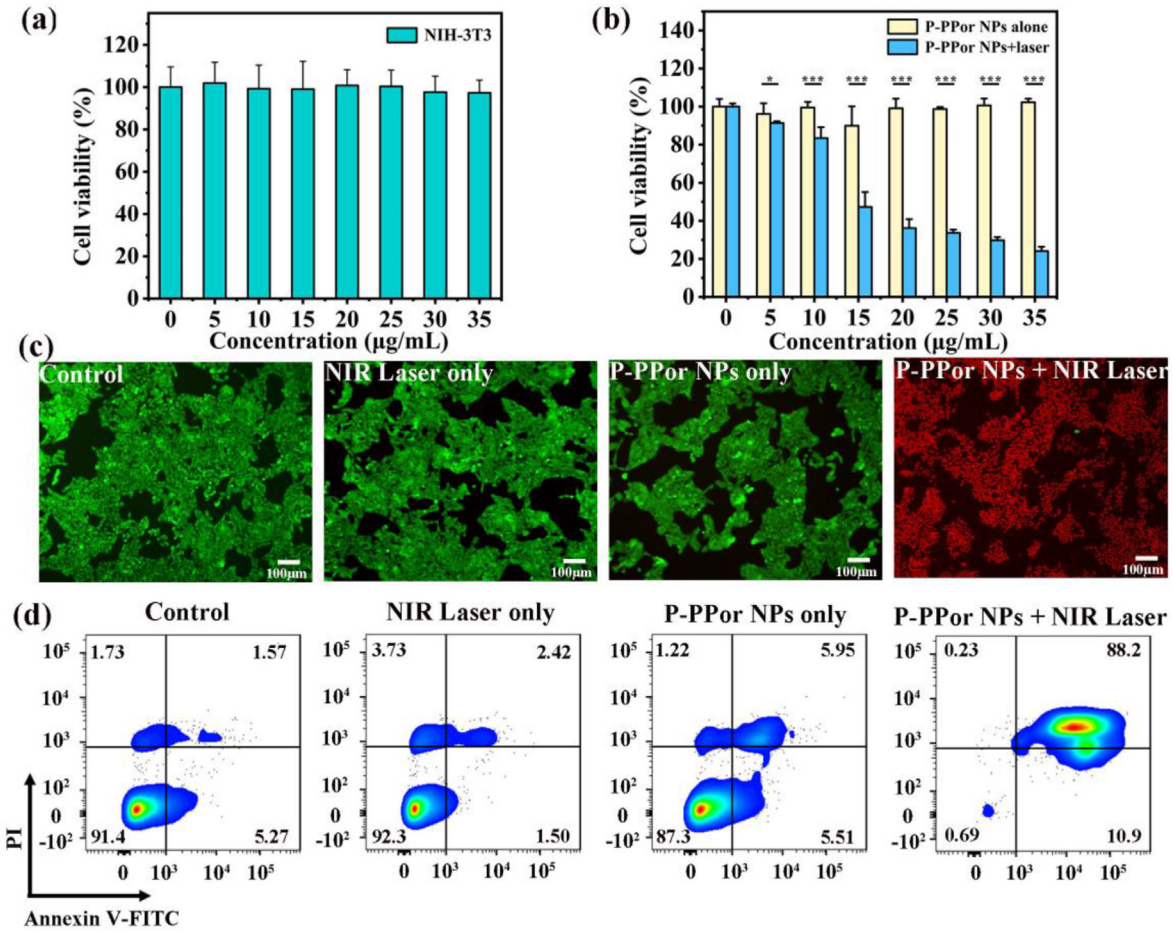


**Fig. 4.** (a) Cell viability of NIH-3T3 cells treated with P-PPor NPs in dark conditions; (b) Cell viability of 4T1 cells treated with P-PPor NPs in dark conditions and with laser irradiation (808 nm, 0.8 W/cm$^2$, 10 min); (c) Fluorescence images of 4T1 cells treated with PBS, laser irradiation, P-PPor NPs and P-PPor NPs + laser irradiation; (d) Flow cytometry analysis of cell apoptosis following the various treatments: I: PBS only, II: PBS + Laser, III: P-PPor NPs, IV: P-PPor NPs + Laser. (The concentration of P-PPor NPs for cancer cell treatment was 15 μg/mL, and the laser power was 0.8 W/cm$^2$, irradiation duration was 10 min).

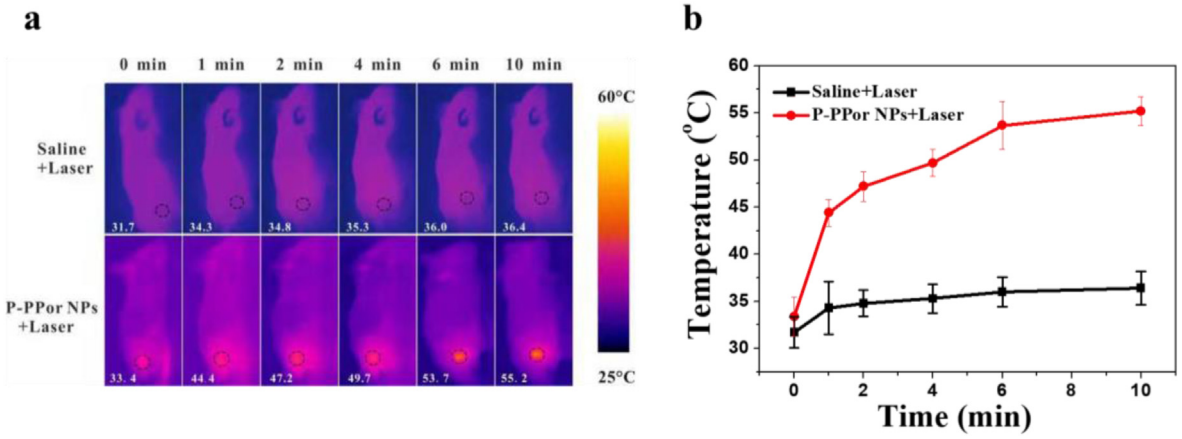


**Fig. 5.** (a) IR thermal images of 4T1 tumor-bearing mice after intravenous injection of PBS or P-PPor NPs followed by the laser irradiation (808 nm, 1.5 W/cm$^2$, 10 min); (b) The temperature change of the tumor sites after intravenous injection of PBS or P-PPor NPs followed by the laser irradiation (808 nm, 1.5 W/cm$^2$, 10 min).

indicated in Fig. 9, no significant variation of the liver and kidney functions (ALT (alanine aminotransferase), AST (aspartate aminotransferase), BUN (blood urea nitrogen) and CRE (creatinine)) was observed among the four groups, indicating the minor effect induced by P-PPor NPs and laser irradiation. Meanwhile, the complete blood panel assay including HGB (hemoglobin), MCHC (mean corpuscular hemoglobin concentration), RBC (red blood cells), HCT (hematocrit), WBC (white blood cells), LYM (lymphocyte), PLT (platelet) and MPV (mean platelet volume) further confirmed P-PPor NPs and laser irradiation did not display any significant biochemical toxicity to the liver and kidneys of mice. Therefore, P-PPor NPs could be applied as an efficient nanoagent against cancer with excellent biocompatibility and high safety.

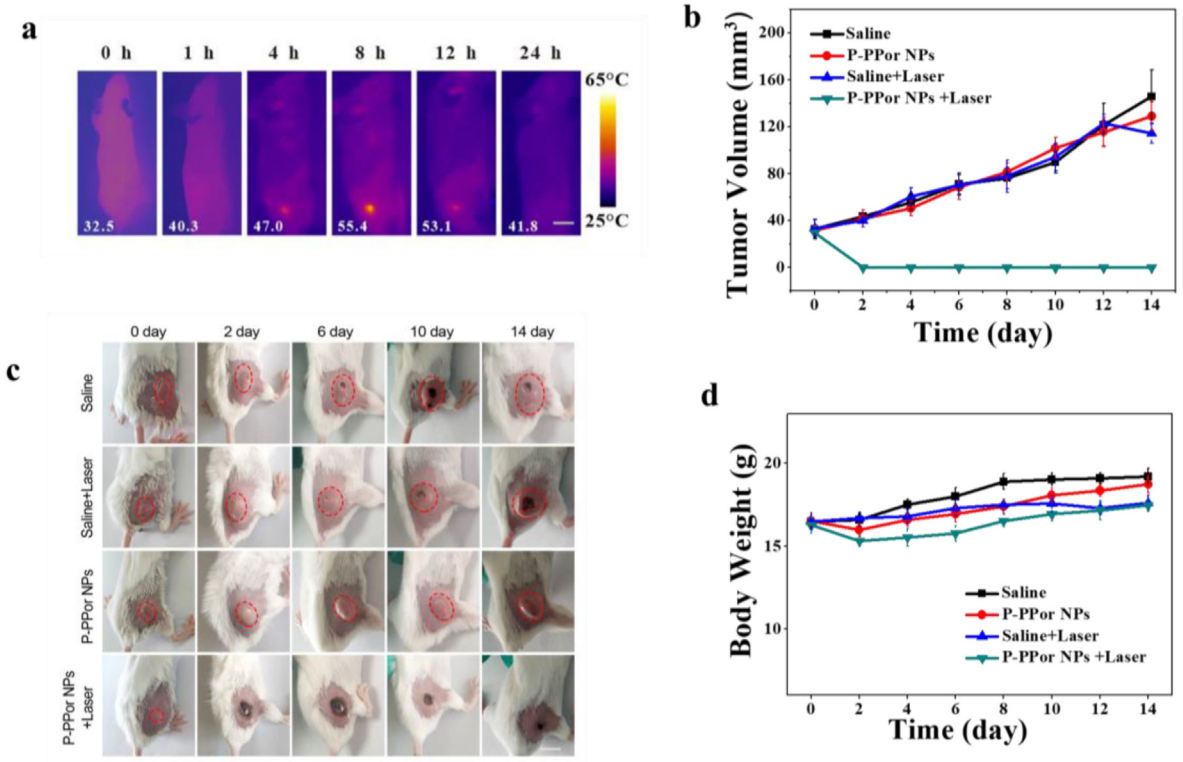


**Fig. 6.** (a) Photothermal imaging in tumor sites after intravenous injection of P-PPor NPs in tumor-bearing mice; (b) The change of tumor volume of mice after different treatments; (c) Photographs indicating the development of tumor at different days in mice upon different treatments; (d) Body weight change of tumor-bearing mice after various treatments. P-values were determined by Student's *t*-test. *P < 0.05, **P < 0.01. Scale bars: 2.5 mm.

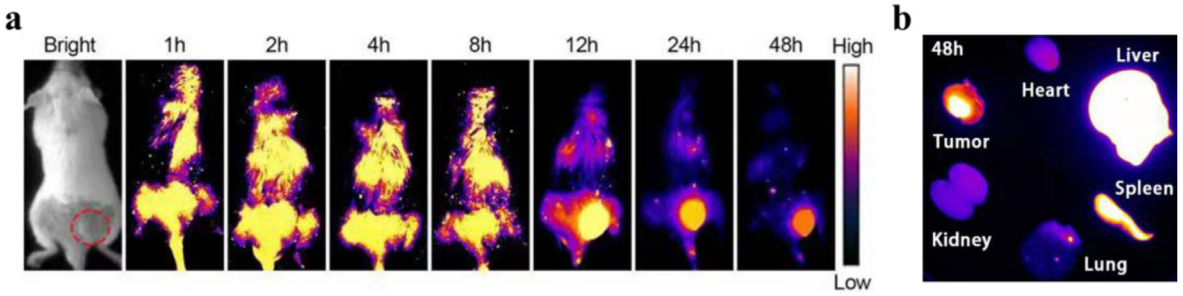


**Fig. 7.** (a) NIR-II fluorescence images of mice injected with 100 μL P-PPor NPs with concentration of 1 mg/mL at different time points; (b) The NIR-II fluorescence signal of the major organs and tumors from mice after 48 h post-injection.

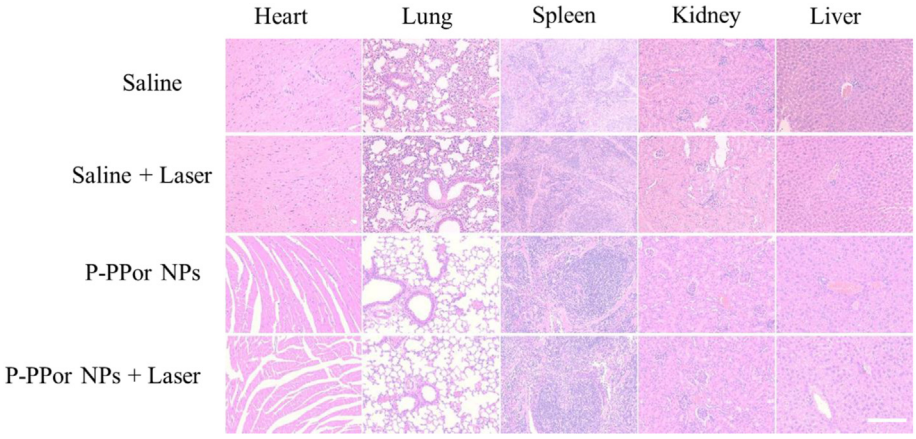


**Fig. 8.** H&E staining of the major organs from the control mice and the mice injected with P-PPor NPs 14 days after PTT treatment. Scale bars: 250 μm.

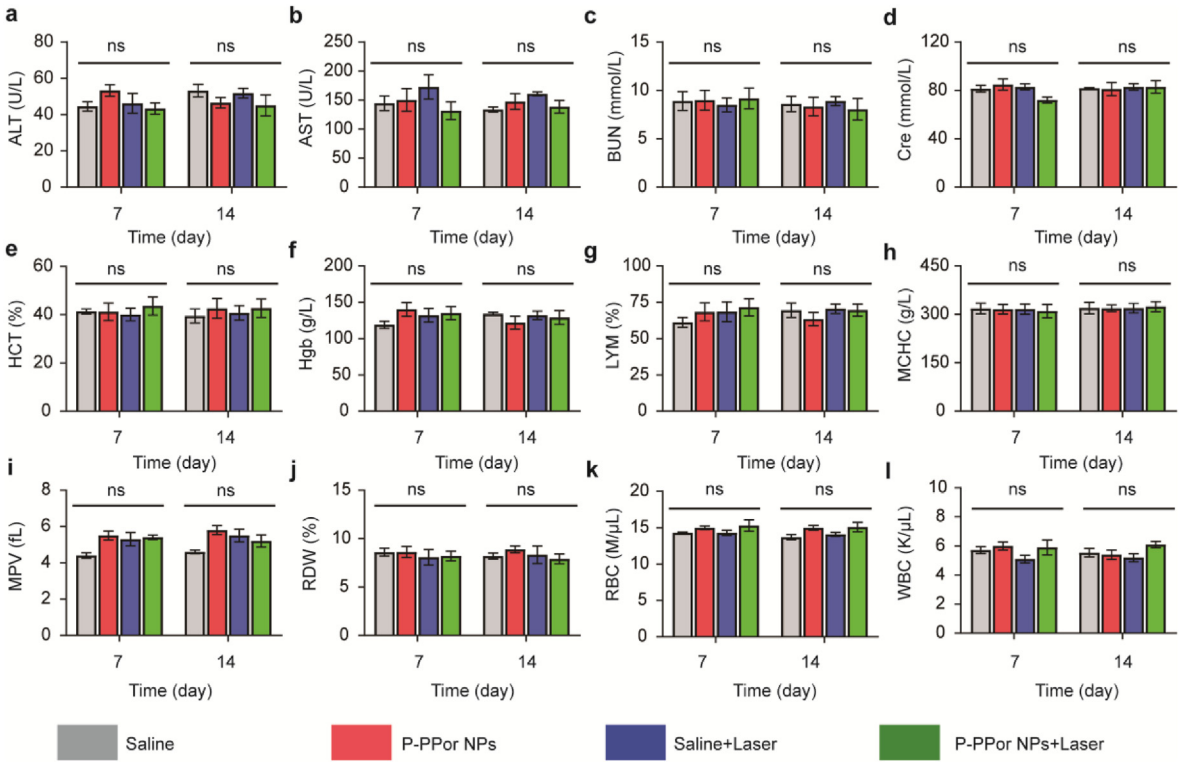


**Fig. 9.** Serum biochemistry and hematology analysis of mice in four groups at 7 and 14 days after different treatments (saline only, P-PPor NPs only, saline + Laser and P-PPor NPs + Laser). (a) ALT, (b) AST, (c) BUN, (d) Cre, (e) HCT, (f) Hgb, (g) LYM, (h) MCHC, (i) MPV, (j) PLT, (k) RBC, (l) WBC. The ns indicates no statistically significant differences.

## 3. Conclusion

In summary, the conjugated porphyrin-based polymer (P-PPor) with D-A structure was synthesized using porphyrin as electron donor and perylene diimide as electron acceptor. P-PPor displayed intense absorbance in the near-infrared region ($\lambda_{abs}$ = 850 nm) and remarkable fluorescence in the NIR-II region ($\lambda_{em}$ = 1015 nm) with fluorescence quantum yield of 2.19%. The amphiphilic polymer was then self-assembled into the related nanoparticles (P-PPor NPs) through reprecipitation method, resulting in the redshift of absorption and fluorescence quenching, facilitating the non-radiative heat generation for photothermal therapy. The PCE of P-PPor NPs was calculated to be 66%, high enough for photothermal cancer therapy. The high biocompatibility, excellent photothermal therapeutic activity and low side effects of P-PPor NPs were proved in vitro and in vivo experiments using 4T1 tumor mode. Moreover, the NIR-II fluorescence imaging in vivo indicated the high distribution of P-PPor NPs in tumor site. Therefore, P-PPor could be used as a promising nanoagent in photothermal clinical applications.

## Credit author statement

Cheng Li: Methodology, Investigation, Formal analysis, Data curation, Writing – original draft. Zijin Luo: Methodology, Investigation, Formal analysis, Data curation. Lixia Yang: Conceptualization, Methodology, Data curation. Jun Chen: Conceptualization, Supervision, Writing – review & editing. Kai Cheng: Methodology, Data curation. Yanan Xue: Methodology, Data curation. Genyan Liu: Methodology, Data curation. Xiaogang Luo: Methodology, Data curation. Fengshou Wu: Conceptualization, Supervision, Funding acquisition, Writing – review & editing.

## Declaration of competing interest

The authors declare that they have no known competing financial interests or personal relationships that could have appeared to influence the work reported in this paper.

## Acknowledgements

This work was supported by National Natural Science Foundation of China (NSFC) (grant no. 21601142), Natural Science Foundation of Hubei Province (grant no. 2018CFB159), Key Project of Scientific Research Project of Hubei Provincial Department of Education (grant no. D20201504), Outstanding Young and Middle-aged Scientific Innovation Team of Colleges and Universities of Hubei Province: “Biomass chemical technologies and materials” (grant no. T201908), Special Projects of the Central Government in Guidance of Local Science and Technology Development in Hubei Province (grant no. 2020ZYYD040), and the second batch of the Key Research and Development Project of Hubei Province (grant no. 2020BAB073).

## Appendix A. Supplementary data

Supplementary data to this article can be found online at https://doi.org/10.1016/j.mtbio.2021.100198.

## References

[1] D. Peer, J.M. Karp, S. Hong, O.C. Farokhzad, R. Margalit, R. Langer, Nanocarriers as an emerging platform for cancer therapy, Nat. Nanotechnol. 2 (2007) 751–760.
[2] J. Chen, J. Ding, W. Xu, T. Sun, H. Xiao, X. Zhuang, X. Chen, Receptor and microenvironment dual-recognizable nanogel for targeted chemotherapy of highly metastatic malignancy, Nano Lett. 17 (2017) 5180.
[3] R.L. Siegel, K.D. Miller, A. Jemal, Cancer statistics, CA A Cancer J. Clin. 66 (1) (2016) 7–30, 2016.
[4] H. Li, L. Yue, M. Wu, F. Wu, Self-assembly of methylene violet-conjugated perylene diimide with photodynamic/photothermal properties for DNA photocleavage and cancer treatment, Colloids Surf. B Biointerfaces 196 (2020) 111351.

[5] H.S. Jung, P. Verwilst, A. Sharma, J. Shin, J.L. Sessler, J.S. Kim, Organic molecule-based photothermal agents: an expanding photothermal therapy universe, Chem. Soc. Rev. 47 (7) (2018) 2280–2297.
[6] A. Espinosa, R. Di Corato, J. Kolosnjaj-Tabi, P. Flaud, T. Pellegrino, C. Wilhelm, Duality of iron oxide nanoparticles in cancer therapy: amplification of heating efficiency by magnetic hyperthermia and photothermal bimodal treatment, ACS Nano 10 (2) (2016) 2436–2446.
[7] Y. Liu, P. Bhattarai, Z. Dai, X. Chen, Photothermal therapy and photoacoustic imaging via nanotheranostics in fighting cancer, Chem. Soc. Rev. 48 (7) (2019) 2053–2108.
[8] X. Li, J.F. Lovell, J. Yoon, X. Chen, Clinical development and potential of photothermal and photodynamic therapies for cancer, Nat. Rev. Clin. Oncol. 17 (11) (2020) 657–674.
[9] R. Chen, J. Zhang, J. Chelora, Y. Xiong, S.V. Kershaw, K.F. Li, P.K. Lo, K.W. Cheah, A.L. Rogach, J.A. Zapien, C.S. Lee, Ruthenium(II) complex incorporated UiO-67 metal-organic framework nanoparticles for enhanced two-photon fluorescence imaging and photodynamic cancer therapy, ACS Appl. Mater. Interfaces 9 (7) (2017) 5699–5708.
[10] J. Qi, Y. Fang, R.T.K. Kwok, X. Zhang, X. Hu, J.W.Y. Lam, D. Ding, B.Z. Tang, Highly stable organic small molecular nanoparticles as an advanced and biocompatible phototheranostic agent of tumor in living mice, ACS Nano 11 (7) (2017) 7177–7188.
[11] J. Zhang, C. Yang, R. Zhang, R. Chen, Z. Zhang, W. Zhang, S.H. Peng, X. Chen, G. Liu, C.S. Hsu, C.S. Lee, Biocompatible D-A semiconducting polymer nanoparticle with light-harvesting unit for highly effective photoacoustic imaging guided photothermal therapy, Adv. Funct. Mater. 27 (13) (2017) 1605094.
[12] F. Wu, L. Chen, L. Yue, K. Wang, K. Cheng, J. Chen, X. Luo, T. Zhang, Small-molecule porphyrin-based organic nanoparticles with remarkable photothermal conversion efficiency for in vivo photoacoustic imaging and photothermal therapy, ACS Appl. Mater. Interfaces 11 (24) (2019) 21408–21416.
[13] F. Wu, J. Chen, Z. Li, H. Su, K.C.-F. Leung, H. Wang, X. Zhu, Red/near-infrared emissive metalloporphyrin-based nanodots for magnetic resonance imaging-guided photodynamic therapy in vivo, Part. Part. Syst. Char. 35 (9) (2018) 1800208.
[14] Y. Cai, P. Liang, Q. Tang, X. Yang, W. Si, W. Huang, Q. Zhang, X. Dong, Diketopyrrolopyrrole-triphenylamine organic nanoparticles as multifunctional reagents for photoacoustic imaging-guided photodynamic/photothermal synergistic tumor therapy, ACS Nano 11 (1) (2017) 1054–1063.
[15] F. Wu, H. Su, Y. Cai, W.-K. Wong, W. Jiang, X. Zhu, Porphyrin-implanted carbon nanodots for photoacoustic imaging and in vivo breast cancer ablation, ACS Appl. Bio. Mater. 1 (1) (2018) 110–117.
[16] J.T. Robinson, S.M. Tabakman, Y. Liang, H. Wang, H.S. Casalongue, D. Vinh, H. Dai, Ultrasmall reduced graphene oxide with high near-infrared absorbance for photothermal therapy, J. Am. Chem. Soc. 133 (17) (2011) 6825–6831.
[17] Y. Jiang, K. Pu, Multimodal biophotonics of semiconducting polymer nanoparticles, Acc. Chem. Res. 51 (8) (2018) 1840–1849.
[18] Y. Lyu, J. Zeng, Y. Jiang, X. Zhen, T. Wang, S. Qiu, X. Lou, M. Gao, K. Pu, Enhancing both biodegradability and efficacy of semiconducting polymer nanoparticles for photoacoustic imaging and photothermal therapy, ACS Nano 12 (2) (2018) 1801–1810.
[19] X. Zhen, J. Zhang, J. Huang, C. Xie, Q. Miao, K. Pu, Macrotheranostic probe with disease-activated near-infrared fluorescence, photoacoustic, and photothermal signals for imaging-guided therapy, Angew. Chem., Int. Ed. Engl. 57 (26) (2018) 7804–7808.
[20] Z. Cao, L. Feng, G. Zhang, J. Wang, S. Shen, D. Li, X. Yang, Semiconducting polymer-based nanoparticles with strong absorbance in NIR-II window for in vivo photothermal therapy and photoacoustic imaging, Biomaterials 155 (2018) 103–111.
[21] X. Li, C.Y. Kim, S. Lee, D. Lee, H.M. Chung, G. Kim, S.H. Heo, C. Kim, K.S. Hong, J. Yoon, Nanostructured phthalocyanine assemblies with protein-driven switchable photoactivities for biophotonic imaging and therapy, J. Am. Chem. Soc. 139 (31) (2017) 10880–10886.
[22] Y. Cai, W. Si, W. Huang, P. Chen, J. Shao, X. Dong, Organic dye based nanoparticles for cancer phototheranostics, Small 14 (25) (2018), e1704247.
[23] Q. Wang, Y. Dai, J. Xu, J. Cai, X. Niu, L. Zhang, R. Chen, Q. Shen, W. Huang, Q. Fan, All-in-One phototheranostics: single laser triggers NIR-II fluorescence/photoacoustic imaging guided photothermal/photodynamic/chemo combination therapy, Adv. Funct. Mater. 29 (31) (2019) 1901480.
[24] T.M. Allen, Ligand-targeted therapeutics in anticancer therapy, Nat. Rev. Cancer 2 (10) (2002) 750–763.
[25] J.M. Warram, E. de Boer, A.G. Sorace, T.K. Chung, H. Kim, R.G. Pleijhuis, G.M. van Dam, E.L. Rosenthal, Antibody-based imaging strategies for cancer, Cancer Metastasis Rev. 33 (2–3) (2014) 809–822.
[26] J.F. Lovell, T.W.B. Liu, J. Chen, G. Zheng, Activatable photosensitizers for imaging and therapy, Chem. Rev. 110 (2010) 2839–2857.
[27] C.S. Jin, J.F. Lovell, J. Chen, G. Zheng, Ablation of hypoxic tumors with dose-equivalent photothermal, but not photodynamic, therapy using a nanostructured porphyrin assembly, ACS Nano 7 (2013) 2541–2550.
[28] M. Yang, J. Deng, D. Guo, Q. Sun, Z. Wang, K. Wang, F. Wu, Mitochondria-targeting Pt/Mn porphyrins as efficient photosensitizers for magnetic resonance imaging and photodynamic therapy, Dyes Pigments 166 (2019) 189–195.
[29] F. Wu, L. Yue, H. Su, K. Wang, L. Yang, X. Zhu, Carbon dots @ platinum porphyrin composite as theranostic nanoagent for efficient photodynamic cancer therapy, Nanoscale Res. Lett. 13 (1) (2018) 357.
[30] S. Zhu, F. Wu, K. Wang, Y. Zheng, Z. Li, X. Zhang, W.K. Wong, Photocytotoxicity, cellular uptake and subcellular localization of amidinophenylporphyrins as potential photodynamic therapeutic agents: an in vitro cell study, Bioorg. Med. Chem. Lett 25 (20) (2015) 4513–4517.
[31] S. Zhu, S. Yao, F. Wu, L. Jiang, K.L. Wong, J. Zhou, K. Wang, Platinated porphyrin as a new organelle and nucleus dual-targeted photosensitizer for photodynamic therapy, Org. Biomol. Chem. 15 (27) (2017) 5764–5771.
[32] X. Lu, P. Yuan, W. Zhang, Q. Wu, X. Wang, M. Zhao, P. Sun, W. Huang, Q. Fan, A highly water-soluble triblock conjugated polymer for in vivo NIR-II imaging and photothermal therapy of cancer, Polym. Chem. 9 (22) (2018) 3118–3126.
[33] P. Sun, Q. Wu, X. Sun, H. Miao, W. Deng, W. Zhang, Q. Fan, W. Huang, J-Aggregate squaraine nanoparticles with bright NIR-II fluorescence for imaging guided photothermal therapy, Chem. Commun. 54 (95) (2018) 13395–13398.
[34] D. Xi, M. Xiao, J. Cao, L. Zhao, N. Xu, S. Long, J. Fan, K. Shao, W. Sun, X. Yan, X. Peng, NIR light-driving barrier-free group rotation in nanoparticles with an 88.3% photothermal conversion efficiency for photothermal therapy, Adv. Mater. 32 (11) (2020), e1907855.
[35] K. He, S. Chen, W. Xu, X. Tai, Y. Chen, P. Sun, Q. Fan, W. Huang, High-stability NIR-II fluorescence polymer synthesized by atom transfer radical polymerization for application in high-resolution NIR-II imaging, Biomater. Sci. 9 (19) (2021) 6434–6443.
[36] Q. Fan, K. Cheng, Z. Yang, R. Zhang, M. Yang, X. Hu, X. Ma, L. Bu, X. Lu, X. Xiong, W. Huang, H. Zhao, Z. Cheng, Perylene-diimide-based nanoparticles as highly efficient photoacoustic agents for deep brain tumor imaging in living mice, Adv. Mater. 27 (5) (2015) 843–847.
[37] S. Zappia, A. de León, M. Alloisio, E. Arias, G. Dellepiane, G. Petrillo, I. Moggio, S. Thea, C. Gallardo-Vega, M. Rodríguez, Optoelectronic properties of a perylene substituted (cholesteryl)benzoateethynylene co-polymer, Mater. Chem. Phys. 147 (3) (2014) 476–482.
[38] A. Zhang, C. Li, F. Yang, J. Zhang, Z. Wang, Z. Wei, W. Li, An electron acceptor with porphyrin and perylene bisimides for efficient non-fullerene solar cells, Angew. Chem., Int. Ed. Engl. 56 (10) (2017) 2694–2698.
[39] K. Nagarajan, A.R. Mallia, K. Muraleedharan, M. Hariharan, Enhanced intersystem crossing in core-twisted aromatics, Chem. Sci. 8 (3) (2017) 1776–1782.
[40] H. Li, L. Yue, L. Li, G. Liu, J. Zhang, X. Luo, F. Wu, Triphenylamine-perylene diimide conjugate-based organic nanoparticles for photoacoustic imaging and cancer phototherapy, Colloids Surf. B Biointerfaces 205 (2021) 111841.
[41] C. Zhu, L. Liu, Q. Yang, F. Lv, S. Wang, Water-soluble conjugated polymers for imaging, diagnosis, and therapy, Chem. Rev. 112 (8) (2012) 4687–4735.
[42] F. Wu, L. Yue, K. Cheng, J. Chen, K.-L. Wong, W.-K. Wong, X. Zhu, Facile preparation of phthalocyanine-based nanodots for photoacoustic imaging and photothermal cancer therapy in vivo, ACS Biomater. Sci. Eng. 6 (9) (2020) 5230–5239.
[43] M. Yang, S. Cao, X. Sun, H. Su, H. Li, G. Liu, X. Luo, F. Wu, Self-assembled naphthalimide conjugated porphyrin nanomaterials with D-A structure for PDT/PTT synergistic therapy, Bioconjugate Chem. 31 (3) (2020) 663–672.
[44] S. Zhang, W. Guo, J. Wei, C. Li, X.J. Liang, M. Yin, Terrylenediimide-based intrinsic theranostic nanomedicines with high photothermal conversion efficiency for photoacoustic imaging-guided cancer therapy, ACS Nano 11 (4) (2017) 3797–3805.